Infrared Emitting Quantum Dots: DNA Conjugation and DNA Origami Directed Self-Assembly

Anirban Samanta, Zhengtao Deng[§], Yan Liu[*]

Department of Chemistry and Biochemistry, and Center for Single Molecule Biophysics,

Biodesign Institute at Arizona State University, 1001 South McAllister Avenue, Tempe,

Arizona 85287-5601, United States

*Corresponding author, email: yan_liu@asu.edu

§ Current address: Research Laboratory of Electronics, Massachusetts Institute of
Technology, Cambridge, MA 02139, USA

Abstract:

QDs that emit in the Infrared (IR) range are of special interest at the moment because of their potential as tissue imaging reagents. Due to autofluorescence from tissues, QDs that emit in the visible range fail to produce good signal to noise ratios. Here we report the production of $Cd_xPb_{1-x}Te$ tertiary-alloyed QDs that emit in the 1100-1300 nm wavelength range, capped with the hydrophilic ligands mercaptopropionic acid (MPA) or glutathione (GSH), together with DNA, as specific surface tags. We observed an interesting dependence of the QD emission peaks on the species of capping ligand used. ICP-MS analysis confirmed that changing the identity of the surface ligand in the reaction mixture shifted the elemental composition of the particles and resulted in different Cd/Pb ratios. Further, DNA directed assembly of the particles onto DNA nanostructures ensures that the particle remains stable in high salt conditions, which is crucial to biological applications.

Keywords: IR emitting quantum dots (QDs), glutathione, alloyed, DNA, self-assembly.

In the past decade, quantum dots (QDs) have emerged as an important subject of research due to their unique optical properties and their potential use in bio-imaging and bio-labeling applications. Tremendous developments have occurred in the synthesis and characterization of various types of QDs.[1-3] Visible light emitting QDs have been commercialized for various labeling purposes. However, the ultimate objective of using QDs for *in vivo* optical fluorescence imaging of human or animal tissues for disease diagnosis and early detection has yet to be realized. Absorption by hemoglobin, melanin, and various proteins, and the auto fluorescence from tissues themselves limit the depth of tissue penetration of any quantum emitter in the visible light range.[4] QDs that emit at near infrared (NIR) and mid-IR regions of the electromagnetic spectrum are superior, since the absorbance and auto fluorescence of biological samples are dramatically lower in this spectral window.[4]

In 2004, Kim et al. demonstrated the use of CdTe/CdSe core/shell QDs emitting in the near IR (850 nm) for real time surgical aids.[5] Water soluble Ag_2S QDs that emit in the near infrared zone has been reported that can be used for targeted imaging of different cell lines and in vivo imaging.[6-10] Alloyed and core-shell QDs that emit in the NIR region have been synthesized in both organic and aqueous media.[11-14] However, in order to achieve QDs that emit in the true IR range, materials with smaller band gaps must be used. Several strategies have been reported to synthesize IR emitting QDs from low band gap materials, including lead chalcogenides (PbS, PbSe), indium arsenide (InAs), mercuric telluride (HgTe), etc.[15-19] Most of these QDs are synthesized in organic media, which is a major drawback for biological applications, as it is necessary to perform a ligand exchange process that is generally detrimental to the photoluminescence quantum

yield (PLQY) of the samples. Water-soluble QDs have been synthesized directly in aqueous buffer, and it is important to further develop these methods to obtain QDs with desirable IR emission, and to explore their bio-functionalization. [20-22]

Here we report the "one-pot synthesis" of IR emitting $Cd_xPb_{1-x}Te$ alloyed QDs functionalized with single stranded DNA (ssDNA). Additionally, we demonstrated DNA origami directed self-assembly of these QDs into discrete nanostructures. Surface modification with DNA has been shown to give the QDs excellent solubility in water and colloidal stability. [23, 24] DNA is a smart molecule with recognition behavior enabled by predictable Watson-Crick base pairing. Displaying specific sequences (such as DNA aptamers) from the nanoparticle allows it to specifically recognize proteins, small molecules or even cell surfaces. [25, 26] Our approach allows us to directly attach DNA oligomers, of any sequence, to the QDs during synthesis. We choose two different materials to make an alloy, one with a moderate band gap, CdTe (1.49 eV), and one with a small band gap, PbTe (0.29 eV). The crystal parameters for CdTe and PbTe are comparable (a_{CdTe} = 0.648 nm and a_{PbTe} = 0.646 nm), but they have different crystal forms: CdTe is zinc blende and PbTe is rock salt. In addition, the diameter of Cd^{2+} ion is significantly smaller than that of Pb^{2+} ion. The formation of alloyed crystals of $Cd_xPb_{1-x}Te$ with 0.85 > x > 0.15 has never been reported before. [27]

We employed a recently reported method to attach DNA to the surface of the alloyed QDs. This method involves the use of DNA with two unique domains, a binding domain that is attached to the surface of the particle, and a recognition domain that is designed to bind other biomolecules such as complementary ssDNA. [26] The DNA backbone of the binding domain is modified with phosphorothioate moieties to impart

high affinity to the inorganic surface, while the backbone of the recognition domain remains the natural phosphate diester bonds. In a typical synthesis following Shih et al., we held the molar ratio between the surface ligands, the sum of the cations (Cd^{2+} and Pb^{2+}) and tellurium at 8:5:1[22], and the ratio between Cd^{2+} and Pb^{2+} at 3:1. Here, two different types of surface ligands, mercaptopropionic acid (MPA) or glutathione (GSH, a tripeptide) were used as the primary ligand, and phosphothioated DNA was used as the secondary ligand. A molar ratio of 40:1 between the primary capping ligands (MPA or GSH) and the secondary DNA ligands was maintained. One interesting observation was that for the same reaction conditions in the absence of DNA, the emission maxima of the resulted QDs were significantly different when the two different primary capping ligands were used. For MPA capped QDs, the emission maximum was at 1310 nm, while for GSH capped QDs, the maximum was at 1110 nm (Fig. 1A-B). The peak position shifted ~ 200 nm, corresponding to a difference in band gap of ~ 170 meV.

We observed that as the concentration of phosphothioated DNA present in the reaction mixture increased from 0 to 100 μM, the emission maximum of the CdPbTe QDs exhibited a significant red shift from 1110 nm to 1215 nm, when the primary ligand was GSH (Fig. 1A). While for the same DNA concentration range, no significant (< 20 nm) emission shift of the QDs was observed when MPA was the primary capping ligand (Fig. 1B). The DNA conjugated QDs were characterized by transmission electron microscopy (TEM) (Fig. 1C-D), which showed the average diameter of the GSH capped QDs was ~10.5±1.1 nm, while the average diameter of the MPA capped QDs was ~5.4±0.6 nm (Fig. 1G-H). A careful examination of TEM images (Fig. 1C) of the GSH capped QDs revealed tiny (~1-2 nm) crystalline domains within the particles (more

enlarged zoom in images shown in Fig. S5), indicating that the particles with an average diameter of ~ 10.5 nm were not single crystals, but rather poly-crystalline with crystal domains in the range of 1-2 nm. Energy-dispersive X-ray spectroscopy (EDS) also confirmed the presence of Cd, Pb, and Te from the QD particles and P from the DNA backbone (Fig. 1E-F). The small S peak originates from the thiol moieties in the primary capping ligands (MPA or GSH), and the phosphorothioated binding domain of the DNA backbone.

The measured sizes of the QDs from TEM images could not sufficiently explain the observed shift of the QD emission maxima, as the smaller MPA capped QDs showed emission peaks at a longer wavelength, which is opposite to the prediction based on quantum confinement effects. One hypothesis is that the presence of unique capping ligands and different amounts of DNA actually cause variations in the composition of the alloyed QDs, even though the reaction mixtures contained the same ratio of the constituent elements (Cd:Pb = 3:1). To test this hypothesis, we determined the ratio of Cd and Pb in the QDs using inductively coupled plasma-mass spectrometry (ICP-MS). The synthesized nanoparticles were first washed and filtered 4 times through Amicon centrifugal devices with 30 kD molecular weight cut off (MWCO) membranes to remove the unreacted precursors, and then redispersed in nanopure water before the ICP-MS measurement. The ICP-MS data (Fig. S1) revealed the resulted QDs contained different ratios of Cd and Pb from what were initially injected into the reaction mixtures. In the absence of DNA, the empirical formula of the GSH and MPA capped particles are $Cd_{0.53}Pb_{0.47}Te$ and $Cd_{0.35}Pb_{0.65}Te$, respectively. The higher content of Pb in the MPA capped QDs is consistent with its longer wavelength emission peak. When the amount of

DNA in the reaction mixture was increased, the GSH capped particles contained significantly more Pb, and the empirical formula changed from $Cd_{0.53}Pb_{0.47}Te$ to $Cd_{0.39}Pb_{0.61}Te$. In contrast, increasing the concentration of DNA in the MPA capped QD mixture did not have a striking effect. Here, the empirical formula changed only slightly, from $Cd_{0.35}Pb_{0.65}Te$ to $Cd_{0.33}Pb_{0.67}Te$. These changes in the chemical composition of the QDs are sufficient to explain the unique emission properties of the QDs obtained, i.e. higher Pb content in the QDs lead to longer emission wavelength.

Powder x-ray diffraction was used to study the obtained nanocrystals (Fig. 2). The peaks were assigned according to the x-ray diffraction patterns of pure cubic phase crystals of PbTe (JCPDS card No. 78-1905) and CdTe (JCPDS Card No. 75-2086). The coexistence of the rock salt (200, 220, 222, 420) and the zinc blende type of diffraction (111, 220, 311) also supports the alloyed structure. There is a significant shift of all of the peaks between the two samples studied: a shift to smaller angles for the sample with MPA capped QDs ($Cd_{0.35}Pb_{0.65}Te$), compared to that of the GSH capped QDs ($Cd_{0.53}Pb_{0.47}Te$). It is known that the radius of the Pb^{2+} ion (133 pm) is larger than that of the Cd^{2+} ion (109 pm) by 22%. This direction of the peak shift is consistent with the Bragg's law ($sin\theta = n\lambda/2d$) that the larger the d, the smaller the diffraction angle. Another observation is the change in the relative peak heights. The unique zinc blende peaks (111, 311) are more prominent in the GSH capped QDs than the MPA capped QDs, also consistent with the higher Cd content in the GSH capped QDs.

One question remained, why was the final elemental composition of the QDs affected by the identity of the capping ligand. We propose that this phenomenon is based on the unique structures of the particular capping ligands, which make them to have

different affinities for the metal cations. MPA is a simple linear molecule with a thiol group that interacts with the QD surface, and a carboxylate group that projects into solution to make the QDs water-soluble. GSH differs from MPA that it has a branched molecular structure and is therefore relatively bulky. In addition, it contains one thiol, two amide bonds, and two carboxylate groups, therefore it may chelate the metal cations and interact with the QD surface through multiple functional groups. Our results seem to indicate that MPA has a stronger affinity for Pb^{2+} than for Cd^{2+}. This is supported by the fact that Pb-S bonds have a higher enthalpy (398 kJ/mol) than Cd-S bonds (208 kJ/mol).[28] Thus, MPA can selectively bring significantly more Pb^{2+} than Cd^{2+} into the QDs as they grow, even in the presence of excess Cd^{2+} in solution, resulting in QDs with longer emission wavelengths. On the other hand, GSH has comparable affinities to these two cations, with an overall affinity to both that is stronger than that of MPA due to the chelating effect. GSH has been successfully used as a capping ligand to synthesize various Cd-based QDs, demonstrating its strong affinity to Cd^{2+}.[11,29] However, quantifying the affinity of GSH to Cd^{2+} and Pb^{2+} cations will require further study.

In both cases, in the presence of phosphothioated DNA, significant amounts of sulfur atoms are added to the reaction mixtures (with ~ 5 phosphothioate groups per DNA strand). Similar to MPA, these phosphothioate groups exhibit stronger affinity for Pb^{2+} than for Cd^{2+}, and thus, do not significantly affect the size or composition of the QDs in the presence of MPA. A small red shift (< 20 nm) in emission was observed, which may be due to the slight increase of Pb content (~ 2%) in the nanocrystals. In the case of GSH capped QDs, the phosphorothioate groups in the DNA backbones have higher affinity for Pb^{2+} than Cd^{2+} (due to favorable Pb-S bond energy), which significantly shifts the

composition of the alloy toward more Pb^{2+} that account for the 100 nm red shift in the emission. Due to stronger affinity of GSH to the metal ions, they may compete with the DNA binding domain on the surface of the QDs and cause less density of DNA on the QDs surfaces, compared to that of the MPA/DNA capped QDs.

The successful conjugation of DNA to the QD surface was demonstrated through site-specific organization of the resulting QDs on DNA nanostructures. DNA origami has proven to be an excellent platform for organizing various nanoparticles into versatile nano-architectures and can be used to fine-tune the distance between the nanoparticles.[24, 30, 31] In a typical assembly process, approximately 200 unique staple strands with rationally designed sequences are mixed with a single stranded genomic DNA scaffold (M13mp18) to create addressable DNA origami structures.[32] At selected addresses, some of the staple strands are extended with DNA sequences complimentary to the binding domain of the DNA displayed from the QDs, so that the QDs are captured at specific locations on the DNA origami. Here, clusters of capture strands (3 per cluster), were arranged 6 nm from one another, on one or all three arms of a triangular origami structure (Fig. 3A). An important requirement of the DNA directed assembly process is the stability of the nanoparticles in aqueous buffers that contain high salt concentrations. For Au or Ag nanoparticles, dense coverage of the surface with DNA is crucial for stability in such conditions.[33] Recently, we reported the synthesis of DNA conjugated core-shell QDs with UV to NIR emission that are stable in high salt concentrations.[24] We did not observe any precipitation of the DNA capped $Cd_xPb_{1-x}Te$ QDs in $1\times TAE-Mg^{2+}$ buffer containing 12.5 mM Mg^{2+} during the 24 hour DNA origami assembly process. This is likely due to the presence of a sufficient number of DNA molecules on the surface of the

particles that render the QDs less prone to aggregation. In contrast, the $Cd_xPb_{1-x}Te$ QDs that contained only the primary capping ligands, GSH or MPA, aggregated overnight in the same buffer.

The assembly of the DNA origami and the QDs was performed in two steps (Fig. 3A). First, the origami was assembled with the required staple strands, the capture strands (each extended with 20 adenine nucleotides at the 5' end), and the circular M13 genomic DNA (3 nM) in a molar ratio of 5:50:1, and annealed from 90°C to 4°C overnight. To remove the excess staple and capture strands, the annealed samples were washed three times and filtered using Amicon filter with 100kD MWCO. The high yield formation of the DNA origami was confirmed by atomic force microscopy (AFM). In the second step, the QDs, each functionalized with ssDNA (20 thymine nucleotides in the DNA recognition domain), was mixed with pre-assembled DNA origami structures and was annealed from 40°C to 4°C over 24 hours. Since the concentration of the QDs is very difficult to determine, we titrated the QD mixtures with a known concentration of the origami, and back calculated the approximate concentration of the particles from the yield of assembled structures. To reduce the probability of cross-hybridized structures, the QD-DNA origami samples were diluted to 0.5 nM with $1 \times TAE\text{-}Mg^{2+}$ buffer before the second annealing step. The self-assembled structures were characterized by AFM and TEM (Fig. 3B).

For the GSH-DNA capped QDs, one particle was positioned site specifically on one side of the triangular origami. AFM analysis revealed ~50% yield of the origami-QD constructs (Fig. 3Bi). AFM height profile measurements indicated QDs with a diameter of ~10.5 nm, in good agreement with the corresponding TEM data (Fig. 3Bv). For MPA-

DNA capped QDs, we organized a total of three QDs, one on each arm of the triangular origami. The assembly yield was approximately 70% (Fig. 3Bii), and the height profile measurements indicated ~5.5 nm diameter particles with a narrow size distribution (Fig. 3Biv). The lower assembly yield of the GSH-DNA capped QDs on the DNA origami could be explained by the larger size and lower surface DNA coverage of these QDs thus lower colloidal stability. For the MPA-DNA encapsulated QDs, incubation with 1×TAE-Mg^{2+} buffer (12.5mM $MgCl_2$) resulted in quenching of fluorescent intensity by 12% with no shift in the emission maxima. Incubating the same QDs with DNA origami in the same buffer cause a 18% decrease of the fluorescence associated with ~10 nm red shift in the emission maxima, compared to the original synthesized QDs. For the GSH-DNA encapsulated QDs, incubation with buffer alone and with DNA origami both causes quenching of fluorescence by 20% and 26%, respectively, and a red shift of ~22 nm in the emission maxima (Figure S6). The significant quenching of the fluorescence intensity and the red shift of the emission maximum could be explained by the slight aggregation of the QDs nanoparticles, which is consistent with the relatively lower assembly yield with DNA origami.

In summary, we demonstrated a simple yet reliable 'one pot synthetic strategy' to conjugate DNA to alloyed $Cd_xPb_{1-x}Te$ QDs that emit in the true IR range. The DNA conjugated particles are stable in aqueous solution with high salt concentration, and are potential candidates for future tissue imaging or labeling applications. Any toxicity due to leaching of cadmium or lead can be prevented by encapsulating the particles with a bio-friendly ZnS shell. Moreover, the successful assembly of the QD particles on DNA

origami to produce discrete nano-architectures further facilitates future applications in

biosensors and biophotonics.

References

1.   X. Michalet, F. F. Pinaud, L. A. Bentolila, J. M. Tsay, S. Doose, J. J. Li, G. Sundaresan, A. M. Wu, S. S. Gambhir and S. Weiss, *Science*, 2005, **307**, 538.
2.   J. K. Jaiswal and S. M. Simon, *Trends in Cell Biology*, 2004, **14**, 497.
3.   I. L. Medintz, H. T. Uyeda, E. R. Goldman and H. Mattoussi, *Nat. Mater.*, 2005, **4**, 435.
4.   V. J. Pansare, S. Hejazi, W. J. Faenza and R. K. Prud'homme, *Chem. Mat.*, 2012, **24**, 81.
5.   S. Kim, Y. T. Lim, E. G. Soltesz, A. M. De Grand, J. Lee, A. Nakayama, J. A. Parker, T. Mihaljevic, R. G. Laurence, D. M. Dor, L. H. Cohn, M. G. Bawendi and J. V. Frangioni, *Nat. Biotechnol.*, 2004, **22**, 93.
6.   Y. Zhang, G. Hong, Y. Zhang, G. Chen, F. Li, H. Dai and Q. Wang, *Acs Nano*, 2012, **6**, 3695.
7.   Y. Du, B. Xu, T. Fu, M. Cai, F. Li, Y. Zhang and Q. Wang, *J. Am. Chem. Soc.*, 2010, **132**, 1470.
8.   S. Shen, Y. Zhang, L. Peng, Y. Du and Q. Wang, *Angew. Chem. Int. Ed.*, 2011, **50**, 7115.
9.   G. Hong, J. T. Robinson, Y. Zhang, S. Diao, A. L. Antaris, Q. Wang and H. Dai, *Angew. Chem. Int. Ed.*, 2012, **51**, 9818.
10. C. Li, Y. Zhang, M. Wang, Y. Zhang, G. Chen, L. Li, D. Wu and Q. Wang, *Biomaterials*, 2014, **35**, 393.
11. A. Samanta, Z. Deng and Y. Liu, *Langmuir*, 2012, **28**, 8205.
12. Z. T. Deng, O. Schulz, S. Lin, B. Q. Ding, X. W. Liu, X. X. Wei, R. Ros, H. Yan and Y. Liu, *J. Am. Chem. Soc.*, 2010, **132**, 5592.
13. G.-X. Liang, M.-M. Gu, J.-R. Zhang and J.-J. Zhu, *Nanotechnology*, 2009, **20**.
14. W. Mao, J. Guo, W. Yang, C. Wang, J. He and J. Chen, *Nanotechnology*, 2007, **18**.
15. S. Keuleyan, E. Lhuillier and P. Guyot-Sionnest, *J. Am. Chem. Soc.*, 2011, **133**, 16422.
16. D. K. Harris, P. M. Allen, H.-S. Han, B. J. Walker, J. Lee and M. G. Bawendi, *J. Am. Chem. Soc.*, 2011, **133**, 4676.
17. J. M. Pietryga, R. D. Schaller, D. Werder, M. H. Stewart, V. I. Klimov and J. A. Hollingsworth, *J. Am. Chem. Soc.*, 2004, **126**, 11752.

18.   M. A. Hines and G. D. Scholes, *Adv. Mater.*, 2003, **15**, 1844.
19.   X. S. Zhao, I. Gorelikov, S. Musikhin, S. Cauchi, V. Sukhovatkin, E. H. Sargent and E. Kumacheva, *Langmuir*, 2005, **21**, 1086.
20.   D. Deng, W. Zhang, X. Chen, F. Liu, J. Zhang, Y. Gu and J. Hong, *Eur. J. Inorg. Chem.*, 2009, 3440.
21.   L. Levina, W. Sukhovatkin, S. Musikhin, S. Cauchi, R. Nisman, D. P. Bazett-Jones and E. H. Sargent, *Adv. Mater.*, 2005, **17**, 1854.
22.   G. H. T. Au, W. Y. Shih, S. J. Tseng and W.-H. Shih, *Nanotechnology*, 2012, **23**.
23.   Q. B. Wang, Y. Liu, Y. G. Ke and H. Yan, *Angew. Chem. Int. Ed.*, 2008, **47**, 316.
24.   Z. Deng, A. Samanta, J. Nangreave, H. Yan and Y. Liu, *J. Am. Chem. Soc.*, 2012, **134**, 17424.
25.   Y.-W. Lin, C.-W. Liu and H.-T. Chang, *Anal. Methods*, 2009, **1**, 14.
26.   N. Ma, E. H. Sargent and S. O. Kelley, *Nat. Nanotechnol.*, 2009, **4**, 121.
27.   P. M. Nikolic, *Br. J. Appl. Phys.*, 1966, **17**, 341.
28.   Z. Deng, S. Pal, A. Samanta, H. Yan and Y. Liu, *Chem. Sci.*, 2013, **4**, 2234.
29.   H. F. Qian, C. Q. Dong, J. F. Weng and J. C. Ren, *Small*, 2006, **2**, 747.
30.   B. Q. Ding, Z. T. Deng, H. Yan, S. Cabrini, R. N. Zuckermann and J. Bokor, *J. Am. Chem. Soc.*, 2010, **132**, 3248.
31.   S. Pal, Z. T. Deng, B. Q. Ding, H. Yan and Y. Liu, *Angew. Chem. Int. Ed.*, 2010, **49**, 2700.
32.   P. W. K. Rothemund, *Nature*, 2006, **440**, 297.
33.   S. J. Hurst, A. K. R. Lytton-Jean and C. A. Mirkin, *Anal. Chem.*, 2006, **78**, 8313.

Figures:
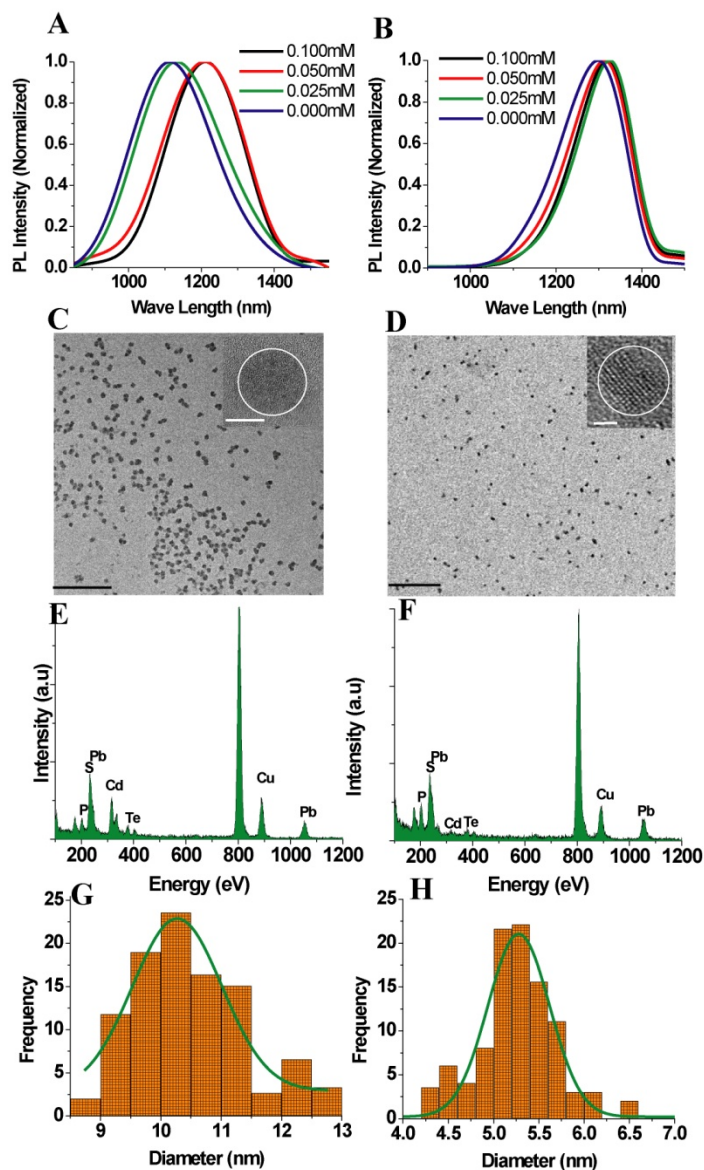
Figure 1. A-B) PL emission spectra of $Cd_xPb_{1-x}Te$ QDs capped with GSH (A) and MPA (B) with varying concentrations of DNA. C-D) TEM image of DNA functionalized $Cd_xPb_{1-x}Te$ QDs capped with GSH (C) and MPA (D). Scale Bars are 100 nm. (Insets in C and D) Respective high resolution TEM images. Scale bars are 5 nm (inset in C) and 2 nm (inset in D). E-F) EDS spectra of DNA conjugated CdPbTe QDs capped with GSH (E) and MPA (F). G-H) Size distribution histogram of the QD samples with average

diameters of 10.5±1.1nm for the GSH capped particles in (G) and 5.4±0.6 nm for the

MPA capped particles in (H).
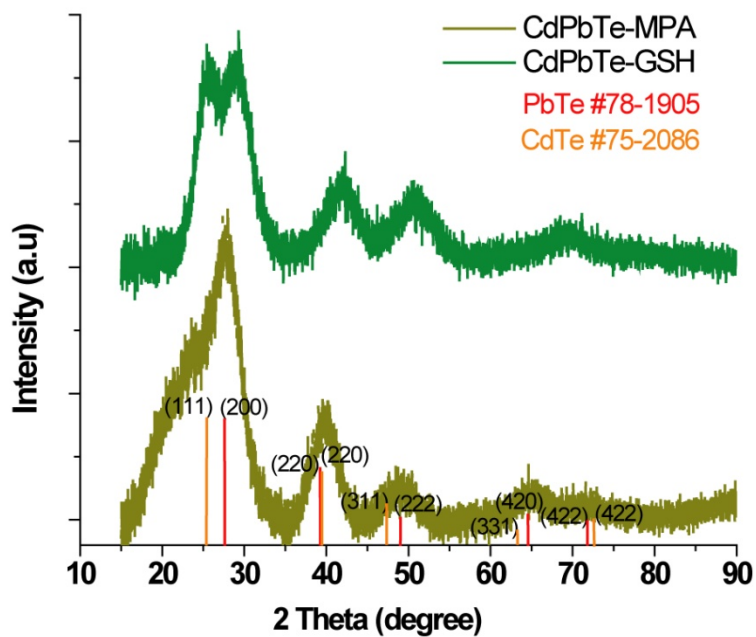
Figure 2. Powder X ray diffraction pattern of $Cd_xPb_{1-x}Te$ QDs encapsulated with GSH

($Cd_{0.52}Pb_{0.48}Te$) (green trace) or MPA ($Cd_{0.35}Pb_{0.65}Te$) (dark yellow trace). The bulk XRD

data of CdTe (orange) and PbTe (red) are also shown as vertical lines for comparison.
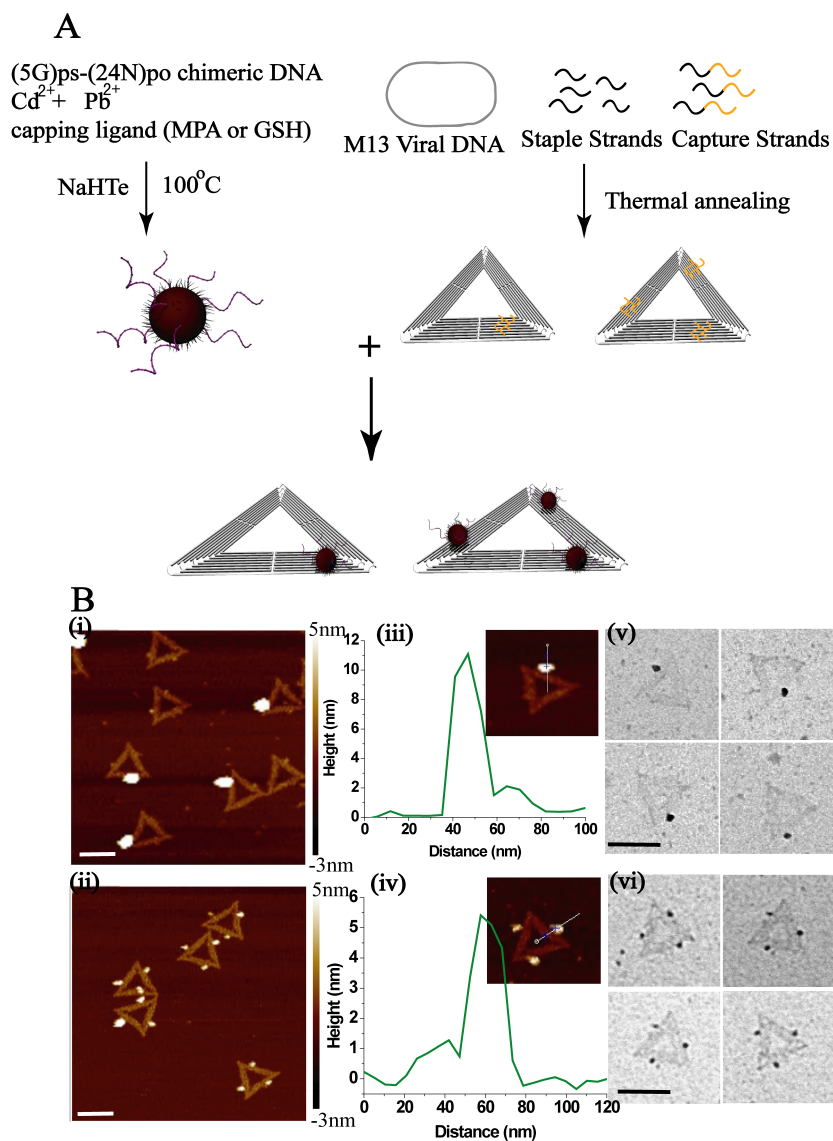
Figure 3. (A) Schematic depicting the synthesis of IR emitting DNA functionalized $Cd_xPb_{1-x}Te$ QDs, the DNA origami and the subsequent self-assembly. (B) i-ii) AFM images of the QDs self-assembled on triangular origami structures, (i) GSH capped (ii) MPA capped. iii-iv) Height profiles from the AFM images of a single QD on the triangular origami as shown in i and ii, respectively. v-vi) Zoom in TEM images of the self-assembled structures (v) GSH capped and (vi) MPA capped, after negative staining with 0.7% uranyl formate solution in water. The scale bar is 100 nm in all images.

TOC

DNA conjugation of infrared emitting hydrophilic QDs and their site-specific organization onto DNA origami.